Nano Research

Open Access

Research Article

Breaking the continuous hydrogen adsorption active sites for boosted urea electrosynthesis

Yuhua Xie[1], Yumei Feng[2], Heng Huang[1], Fang Luo[3] ✉, Sergey A. Grigoriev[4,5], Xiaoyang Fu[2] ✉, Jin Zhang[2,6], and Zehui Yang[1] ✉

[1] College of Materials and Chemical Engineering, China Three Gorges University, Yichang 443002, China
[2] State Key Laboratory of Advanced Waterproof Materials, School of Materials Science and Engineering, Peking University, Beijing 100871, China
[3] State Key Laboratory of New Textile Materials & Advanced Processing Technology, College of Materials Science and Engineering, Wuhan Textile University, Wuhan 430200, China
[4] National Research University "Moscow Power Engineering Institute", 14, Krasnokazarmennaya St., 111250 Moscow, Russia
[5] National Research Centre "Kurchatov Institute", 1, Akademika Kurchatova Sq., 123182 Moscow, Russia
[6] Beijing Science and Engineering Center for Nanocarbons, Beijing National Laboratory for Molecular Sciences, College of Chemistry and Molecular Engineering, Peking University, Beijing 100871, China

Cite this article: *Nano Research*, **2026**, *19*, 94908834. https://doi.org/10.26599/NR.2026.94908834

ABSTRACT: The efficient electrosynthesis of urea from CO_2 and NO_3^- relies on the suppression of the competitive hydrogen evolution reaction (HER), especially the Tafel and Heyrovsky steps. We designed CuNi alloyed structure encapsulated into nitrogen doped carbon nanotubes (CuNi-NCNT) for superior urea electrosynthesis. The interstitial Cu atom breaks the successive hydrogen binding active sites, Ni atoms, as NO_3^- and CO_2 strongly adsorb on Cu sites, hindering the Tafel step of HER. Besides, due to the steric effect, the Heyrovsky step is also restrained. Thus, the HER catalysis is well suppressed, leading to a high Faradaic efficiency (33.6%) of urea electrochemical synthesis for CuNi-NCNT at −0.4 V vs. reversible hydrogen electrode (RHE) associated with yielding rate of 5.3 mmol·h^{-1}·g$_{cat}^{-1}$, boosted by factors of 6.7 and 4.4 with relative to Ni-NCNT and metallic Cu, respectively. The *in-situ* Raman spectroscopy and integrated crystal orbital Hamilton population (ICOHP) theoretical calculation indicate that Ni sites strongly adsorb hydrogen atom for hydrogeneration, while CO_2 and NO_3^- are electrochemically bound with Cu atoms, synergistically contributing to the efficient urea formation. Moreover, the *in-situ* Raman spectroscopy suggests the reaction pathway of urea electrosynthesis via the formation of *NH_2 and *CO species from NO_3^- and CO_2. Consequently, a lowered energy barrier for C–N coupling (0.55 eV) can be achieved on CuNi compared to Cu(111) and Ni(111). This work offers significant insights into the critical roles of Cu and Ni in urea electrosynthesis and promotion in catalytic activity in Cu-system.

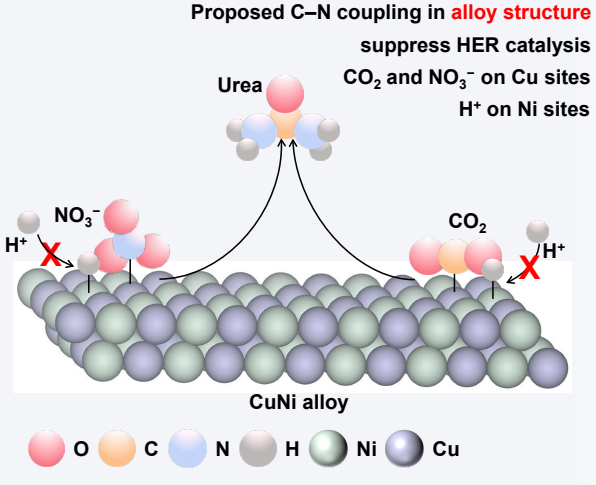

KEYWORDS: urea electrosynthesis, hydrogen evolution reaction, CuNi alloy, C–N coupling

1 Introduction

Urea is an important fertilizer in modern agriculture, supporting the expanding population associated with the growing requirements of food. Moreover, urea has also been utilized as raw material for medicines, plastics, textiles, etc. [1–4]. Carbon dioxides (CO_2) and ammonia (NH_3) react via Bosch–Meiser process at high temperature (200 °C) and pressure (200 MPa) to generate urea due to the difficulty in C–N coupling [5–7]. Additionally, ammonia is normally synthesized via the energy-consuming Haber–Bosch process ($N_2 + 3H_2 \rightarrow 2NH_3$), which also requires harsh conditions because of the stable N≡N bond [8–11]. More recently, the

Received: March 19, 2026; **Revised:** May 6, 2026
Accepted: May 12, 2026

✉Address correspondence to Fang Luo, luofang04@gmail.com; Xiaoyang Fu, fuxy@pku.edu.cn; Zehui Yang, yeungzehui@gmail.com

electrochemical reduction of nitrate to form ammonia in aqueous electrolyte was tremendously reported [12–16]. Thus, with the introduction of CO_2 into the electrolyte, the urea can be electrochemically synthesized at ambient condition.

The electrochemical synthesis of urea relies on the C–N coupling from the reduction of NO_3^- to $*NO_2$ and CO_2 to *CO intermediates; therefore, the hydrogenation of NO_3^- and CO_2 to remove oxygen atom is highly essential, which demands abundant adsorbed hydrogen atoms, and the hydrogen evolution reaction (HER) should be well suppressed [17–19]. Based on the HER catalysis process, the Volmer step is highly demanded for urea synthesis and the relative Heyrovsky or Tafel step should be prevented [20]. As Tafel step is more favorable for HER, breaking the continuous HER active center is considered as the promising strategy to delay the HER catalysis [21]. In this aspect, bimetallic materials have been investigated as high-performance electrocatalyst for urea electrosynthesis, such as Pd-Cu [22, 23], Ag-Cu [24, 25], Au-Cu [26, 27], and Cu-Bi [28, 29], due to the high capability of Cu for the adsorption of NO_3^- and CO_2 [30, 31]; besides, the binding strength between Cu and hydrogen atom is relatively weak. However, owing to the limited storage of noble metals, these electrocatalysts are not economically feasible for real application of urea electrosynthesis; furthermore, the noble-metals normally exhibit higher HER activity, resulting in a low Faradaic efficiency (FE) of urea electrosynthesis [9, 32, 33]. We reported nickel nanoparticle encapsulated into nitrogen doped carbon nanotubes (Ni-NCNT) performing superior HER activity due to the favorable hydrogen binding strength for Ni atom, whose electronic structure was adjusted by nitrogen and carbon atoms [34, 35]. Therefore, the introduction of Cu to Ni-NCNT could break the continuous HER active sites and be potentially utilized as robust electrocatalyst for urea electrosynthesis.

In this work, we synthesized CuNi-NCNT electrocatalyst via pyrolysis method. The HER activity of the constructed CuNi-NCNT was well suppressed due to the incorporation of Cu atom. The CO_2 and NO_3^- species were co-adsorbed on the Cu atom; thus, the continuous hydrogen adsorption sites (Ni) were broken, preventing Tafel step of HER; moreover, the adsorbed NO_3^-/CO_2 on Cu also prohibited the hydrogen adsorption on Ni atom ascribed to the steric effect, decelerating Heyrovsky step of HER shown in Fig. 1. The Faradaic efficiency for urea electrosynthesis was 33.6% for CuNi-NCNT at −0.40 V vs. RHE and a yielding rate was 5.3 $mmol \cdot h^{-1} \cdot g_{cat}^{-1}$, which was boosted by 3.6 and 3.2 times than Ni-NCNT and metallic Cu, respectively. The *in-situ* Raman spectroscopy test and COHP calculation revealed that hydrogen absorbed on Ni atoms and NO_3^-/CO_2 strongly adsorbed on Cu atoms, respectively. Density functional theory (DFT) calculations further demonstrated the CuNi-NCNT not only suppressed Tafel and Heyrovsky steps during HER but also promoted the formation of C–N bond, leading to a robust activity and selectivity towards urea electrosynthesis.

2 Experimental section

2.1 Preparation of CuNi-NCNT and Ni-NCNT electrocatalysts

Firstly, 1 g of copper chloride dihydrate ($CuCl_2 \cdot 2H_2O$, ≥ 99%) and 1 g of nickel chloride hexahydrate ($NiCl_2 \cdot 6H_2O$, ≥ 98%) were weighed and added to 60 mL of a methanol-ethanol mixed solution (methanol: CH_3OH, ≥ 99.5%; ethanol: C_2H_5OH, ≥ 99.7%). After complete dissolution, 5 g of melamine ($C_3H_6N_6$, content ≥ 99%, Sinopharm Chemical Reagent Co., Ltd.) was weighed and dispersed into the solution. The resultant was stirred for 10 h (500 rpm, 80 °C). After complete evaporation, the residue was ground into powder. Then the powder was calcined in a tube furnace under a flowing N_2 atmosphere (first held at 500 °C for 2 h, then held at 800 °C for 2 h, with a heating rate of 5 $°C \cdot min^{-1}$). The resulting sample was CuNi-NCNT. The preparation method for the control sample was identical to the above, except only 1 g of -$NiCl_2 \cdot 6H_2O$ was added, yielding Ni-NCNT. NCNT was synthesized with the nitric acid treatment of CuNi-NCNT to remove CuNi.

2.2 Characterizations

X-ray diffraction (XRD) patterns were recorded using a Bruker D8 Advance diffractometer with Cu-Kα radiation (λ = 1.5406 Å). The surface morphology was observed via a scanning electron microscopy (SEM, SU8010). The elemental information was determined via X-ray photoelectron spectroscopy (XPS, ESCALB 250) with an Al Kα X-ray source. Transmission electron

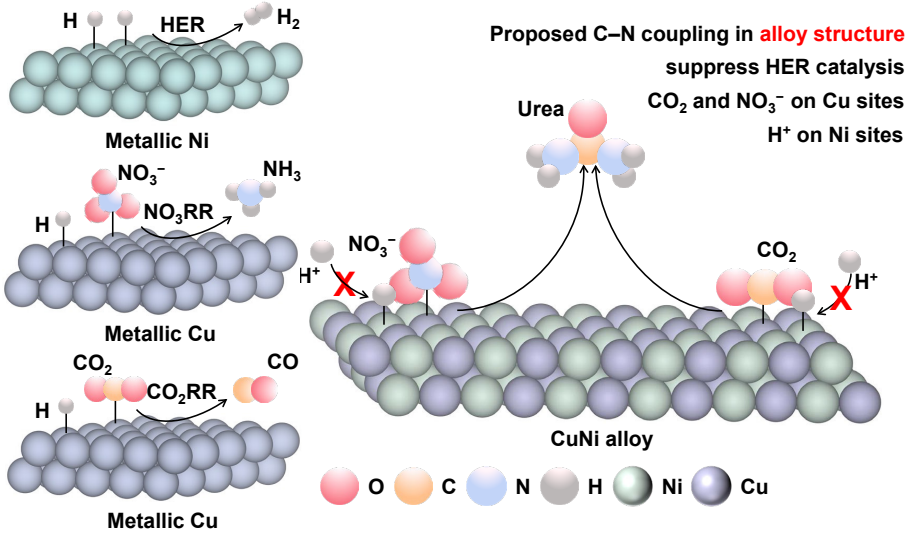

Figure 1 Scheme of the urea electrosynthesis on CuNi alloy structure.

microscopy (TEM) tests were carried out using a Talos F200x microscope. Raman spectroscopy (i-Raman Plus) was obtained from BWS465-532H with a 532 nm excitation laser. ASAP 2460 equipment was used for N_2 adsorption–desorption analysis.

3 Results and discussions

3.1 Fundamental characterizations

The as-synthesized electrocatalysts were first characterized via XRD (Fig. 2(a)) and sharp diffraction peaks were observed, demonstrating the high crystallinity of the formed Ni-NCNT and CuNi-NCNT. The diffraction peak at 44.4° was the dominant (111) facet for metallic Ni from JCPDS No. 01-1258. Compared to Ni-NCNT, the dominant XRD peak was negatively shifted due to the different atomic radius, confirming that the alloy formation and tensile strain were suggested [36]. In comparison, metallic Cu was also synthesized and confirmed by the diffraction peaks at 43.3° 50.4°, and 74.1° from JCPDS No. 04-0836. The molar ratio between Cu and Ni was 3:1 from inductively coupled plasma-mass spectrometry (ICP-MS) test. As shown in Fig. S1 in the Electronic Supplementary Material (ESM), the electronic interaction between Cu and Ni was further studied by XPS. Initially, the C 1s XPS peak was deconvoluted to C=N (286.3 eV), C–C (284.8 eV), O=C–O (292.1 eV), and C–N (288.7 eV) species (Fig. S2 in the ESM), verifying the introduction of nitrogen dopants to carbon skeleton. Consequently, the fitted N 1s spectra shown in Fig. S3 in the ESM suggested the presence of oxidized, graphitic, pyrrolic, and pyridinic N moieties at 407.2, 404.9, 403.8, and 402.0 eV stemming from the melamine precursor, respectively. As displayed in Fig. 2(b), Ni 2p XPS peak was mainly composed of Ni $2p_{1/2}$ and Ni $2p_{2/3}$ at 870.1 and 852.5 eV, respectively, while a low percentage of Ni^{2+} specie was present in Ni-NCNT and CuNi-NCNT due to the formation of Ni–N–C structure at heterointerface between metallic Ni and NCNT [35]. Importantly, the introduction of Cu atoms showed an negligible change in Ni^{2+} content (Fig. 2(c)) [37]. Additionally, the Cu 2p peak was also recorded and fitted (Fig. 2(d)) with predominantly metallic Cu^0, similar to that of metallic Cu [38, 39]. Differently, the specific surface areas were 78.8 and 48.5 $m^2 \cdot g^{-1}$ for CuNi-NCNT and Ni-NCNT, respectively (Fig. 2(e)). The increment in specific surface area was due to the utilization of $CuCl_2$ as precursor. The generated chlorine during synthesis etched NCNT, contributing to a higher specific surface area. In order to confirm this point, the Raman spectroscopy (Fig. 2(f)) demonstrated I_D/I_G ratio of 0.98 for CuNi-NCNT, which was 1.7-fold higher than Ni-NCNT (0.59), indicating that more defective sites were created for CuNi-NCNT. The increased I_D/I_G ratio of CuNi-NCNT demonstrated more defects in NCNT, favorable for the diffusion of reactant and production [40].

As shown in Fig. 3(a), nanotube with diameter of ~ 100 nm was observed for Ni-NCNT and the formation of NCNT structure originated from the catalysis of melamine by Ni nanoparticle at high temperature. With the addition of $CuCl_2$, nanotube was still observed for CuNi-NCNT shown in Fig. 3(b). Meanwhile, the TEM images in Figs. 3(c) and 3(d) further confirmed the formation with CuNi nanoparticles confined inside the nanotubes. The lattice spacing of CuNi nanoparticle was 0.197 nm for (111) crystal plane (Fig. 3(e)), which was slightly higher than that of Ni-NCNT shown in Fig. S4 in the ESM, in line with the XRD measurements. The lattice spacing of 0.341 nm confirmed the formation of graphitic carbon and Ni(111) facet was confirmed by lattice spacing of 0.20 nm. It was found that Cu and Ni elements were uniformly dispersed in CuNi nanoparticle encapsulated into NCNT from the energy dispersive X-ray spectroscopy (EDS) mapping (Fig. 3(f)).

3.2 Urea electrosynthesis

The performance of urea electrosynthesis was tested in 0.05 M H_2SO_4 electrolyte with additional KNO_3 and CO_2 purging. In Fig. S5 in the ESM, the current density increased after adding KNO_3 to electrolyte for metallic Cu due to the capability of nitrate reduction

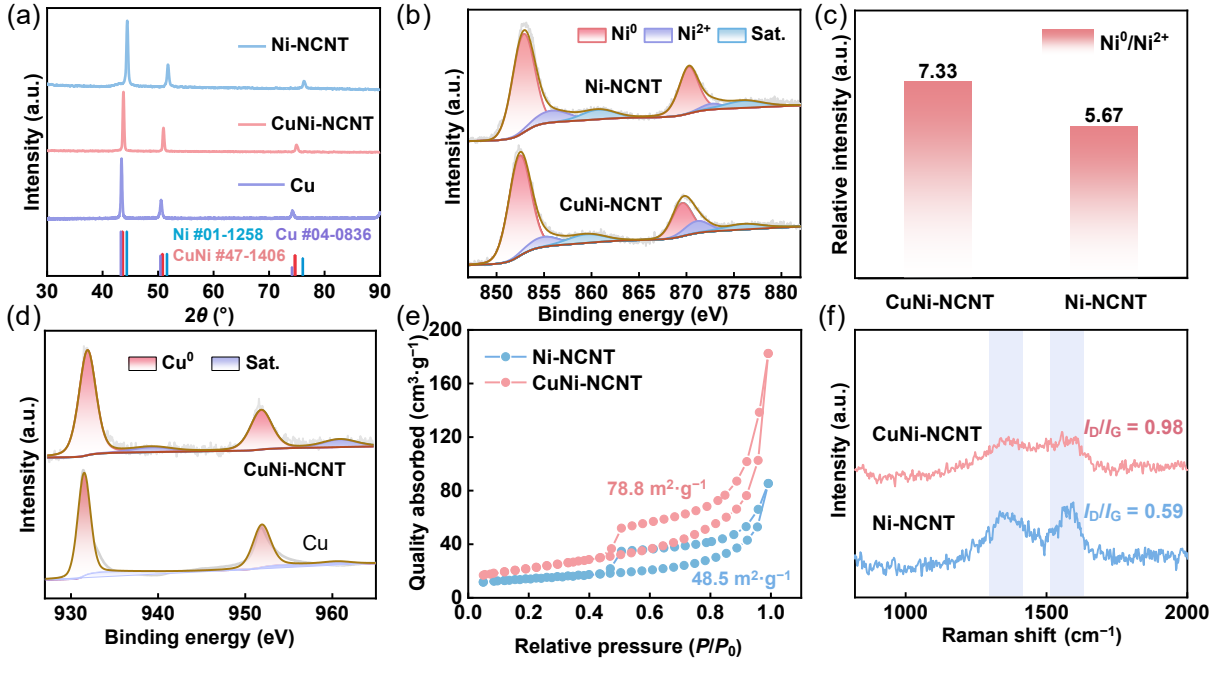

Figure 2 (a) XRD patterns of metallic Cu, Ni-NCNT, and CuNi-NCNT. (b) Deconvoluted Ni 2p, (c) relative ratios of relevant Ni species, and (d) deconvoluted Cu 2p peaks of Cu and CuNi-NCNT. (e) N_2 adsorption and desorption isothermal curves and (f) Raman spectra for Ni-NCNT and CuNi-NCNT.

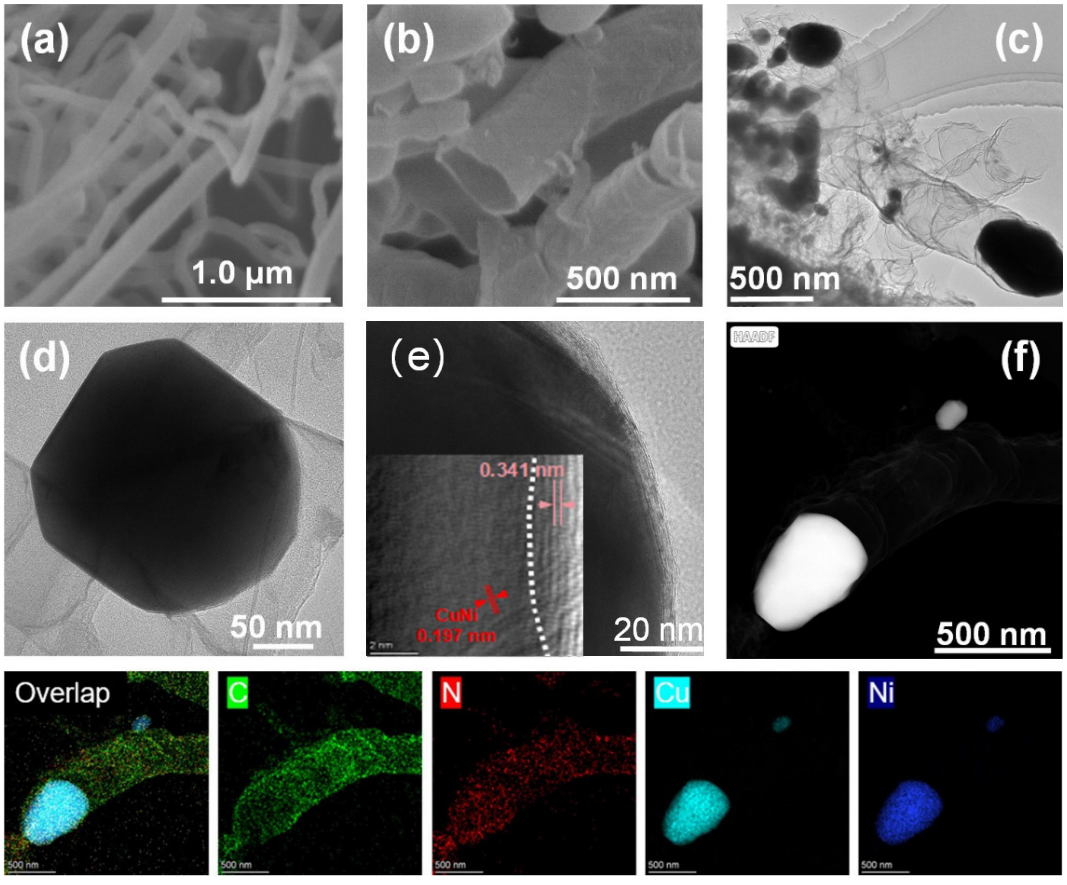

Figure 3 ((a) and (b)) SEM images of (a) Ni-NCNT and (b) CuNi-NCNT. ((c) and (d)) TEM images at different magnifications and (e) HR-TEM images of CuNi-NCNT, along with (f) high-angle annular dark-field (HAADF) and elemental EDS mapping (C, N, Cu, and Ni).

reaction [41, 42]; while, the current density was decreased after purging with CO_2 because of the suppression of nitrate reduction reaction. Similar trends were also found for Ni-NCNT (Fig. 4(a)) and CuNi-NCNT (Fig. 4(b)). As HER is the competitive reaction for urea electrosynthesis, it was noticed that CuNi-NCNT exhibited much lower HER performance than metallic Cu and Ni-NCNT in Fig. S6(a) in the ESM. The introduction of Cu atom to Ni-NCNT effectively suppressed the HER performance, which was beneficial for the urea electrosynthesis [43, 44]. The optimized HER performance of Ni-NCNT suggested that Ni could serve as the most active centers for hydrogen adsorption, while in the CuNi alloy structure, the continuous hydrogen adsorption sites from Ni could be destroyed [35]; therefore, the HER activity of CuNi-NCNT was well suppressed. As shown in Figs. S6(b) and S6(c) in the ESM, the HER performance of Ni-NCNT was largely decayed after Cu incorporation. To reveal the suppressed HER catalysis, electrochemical impedance spectroscopy (EIS) has been performed and fitted. Constant phase angle element (CPE) normally represents the adsorption of reaction intermediates (H^+). It was found the CPE value decreased from 3.42 to 1.12 mF after the introduction of Cu; thereby, the Cu atoms in CuNi alloy suppressed the adsorption of hydrogen ions. As shown in Fig. S7 in the ESM, NCNT exhibited almost no catalytic activity in CO_2-purged 0.05 M H_2SO_4 with 200 ppm KNO_3; therefore, the robust performance of urea electrosynthesis originated from the inside CuNi alloy. Furthermore, the current density of CuNi-NCNT increased by ~ 8.5-fold in 0.05 M H_2SO_4 + 200 ppm KNO_3 electrolyte at −0.6 V vs. RHE, suggesting the high activity for nitrate reduction reaction on CuNi alloy. With the introduction of CO_2, the current density was seriously decayed for CuNi-NCNT; for instance, the current density decreased by 35.7% at −0.6 V vs. RHE; however, the values were only 22.1% and 15.2% for metallic Cu and Ni-NCNT, respectively. Thus, CO_2 reduction was more prone to occur on Cu atom. In order to confirm this point, the current density was higher with CO_2 purging for metallic Cu than Ni-NCNT; thus, CO_2 was more susceptible to electrochemical adsorption and conversion on Cu atoms (Fig. S8 in the ESM). As shown in Fig. S9 in the ESM, CuNi-NCNT exhibited a comparably lower charge transfer resistance (R_{ct}) than Ni-NCNT, implying its better catalytic activity. In addition, the double layer capacitance (C_{dl}) was evaluated from cyclic voltammetry curves (Fig. S10 in the ESM). C_{dl} value reached 2.1 mF·cm^{-2} for CuNi-NCNT, increased by 31% than Ni-NCNT (1.6 mF·cm^{-2}, Fig. 4(c)), due to the incorporation of Cu atoms contributing to more electrochemically active sites. To further study the selectivity towards urea electrosynthesis, the products in electrolyte were analyzed by ultraviolet–visible (UV–vis) spectroscopy testing. Initially, the standard calibration curves, regarding concentration vs. intensity, were established for NH_4^+ (Fig. S11 in the ESM), NO_2^- (Fig. S12 in the ESM), and urea (Fig. S13 in the ESM). The electrolytes were analyzed after 2 h of electrolysis at various applied potentials, as shown in Fig. 4(d). Based on the intensity of UV–vis spectroscopy at 525 nm (Fig. 4(e)), the FE of urea electrosynthesis reached 33.6% for CuNi-NCNT at −0.40 V vs. RHE shown in Fig. 4(f), which was boosted by a factor of 6.7 and 4.4 than Ni-NCNT (Fig. S14 in the ESM) and metallic Cu (Fig. S15 in the ESM) calculated from UV–vis

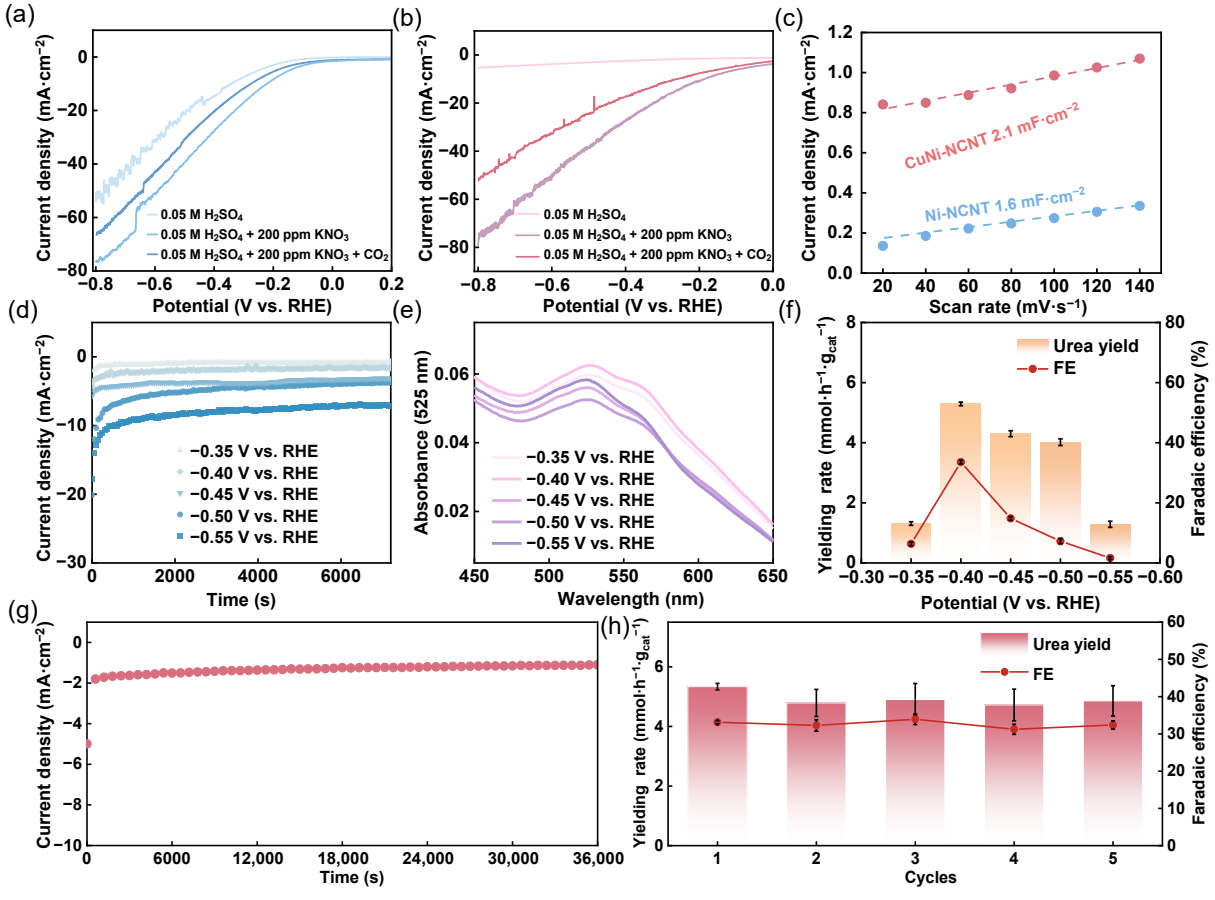

Figure 4 ((a) and (b)) Electrochemical performance of (a) Ni-NCNT and (b) CuNi-NCNT in urea synthesis within H-type electrolyzers. (c) The double layer capacitances spectroscopies of Ni-NCNT and CuNi-NCNT. (d) *i*–*t* curves of CuNi-NCNT at different reduction potentials over 2 h. (e) UV–vis spectroscopy of collected electrolyte at 525 nm and (f) measured urea yield and Faraday efficiency. (g) *i*–*t* curve (10 h) of CuNi-NCNT at −0.4 V vs. RHE and (h) urea yield and Faradaic efficiency at different time points during the process.

spectroscopy, respectively. Besides, the urea yielding rates were 5.3, 1.47, and 1.67 mmol·h^{-1}·g$_{cat}^{-1}$ for CuNi-NCNT, Ni-NCNT, and metallic Cu, respectively. It was reasonable that Ni-NCNT exhibited an ultralow FE for urea electrosynthesis because of lower capability for CO_2 reduction of Ni. In case of metallic Cu, due to its considerable HER performance, the FE for urea electrosynthesis was also suppressed. To show the importance of CuNi alloy structure, the physically mixed electrocatalyst, denoted as Cu + Ni-NCNT, was tested. As shown in Fig. S16 in the ESM, the FE value of Cu + Ni-NCNT was lower than the counterpart of CuNi-NCNT, implying the importance of CuNi alloy structure. Since the nitrate can be electrochemically converted to ammonia and NO_2^-, the FE of ammonia was also calculated. Based on the UV–vis spectroscopy at 655 nm (Fig. S17 in the ESM), the FEs for ammonia were calculated to 23.2%, 10.2%, and 72.7% at −0.40 V vs. RHE for CuNi-NCNT, Ni-NCNT, and metallic Cu, respectively (Fig. S18 in the ESM). Similarly, the NO_2^- concentration was also tested by UV–vis spectroscopy (540 nm, Fig. S19 in the ESM) and the corresponding FE values were 1.57%, 0.72%, and 1.89% for CuNi-NCNT, Ni-NCNT, and metallic Cu, respectively (Fig. S20 in the ESM). The stability was also estimated and stable current density was obtained during 10 h (Fig. 4(g)). The electrolyte was tested with UV–vis spectroscopy every 2 h (Fig. S21 in the ESM). From the TEM test shown in Fig. S22 in the ESM, the superior structural stability was confirmed for CuNi-NCNT. Based on the UV spectroscopy, the FE and urea production rate were 34.1% and 5.25 mmol·h^{-1}·g$_{cat}^{-1}$ for CuNi-NCNT shown in Fig. 4(h), respectively, illustrating the robustness in urea electrosynthesis. Compared to recently reported electrocatalysts (Table S1 in the ESM), CuNi-NCNT showed a high FE during urea electrosynthesis.

To confirm the superior catalytic activity towards urea electrosynthesis, the catalysis was measured with and without CO_2 [45]. From the UV–vis spectroscopy (Fig. S23 in the ESM), a similar intensity was observed for the blank sample and the electrolyte without CO_2, indicating the solid demand for CO_2 for the urea electrosynthesis. Additionally, the isotope experiment was carried out. As shown in Fig. 5(a), two nuclear magnetic resonance (NMR) peaks at 5.62 and 5.79 ppm were observed using $K^{15}NO_3$ as nitrogen source; however, only one intensity peak at 5.70 ppm was detected with $K^{14}NO_3$, highlighting that KNO_3 was the nitrogen source for urea electrosynthesis. Not surprisingly, the generated NH_4^+ also showed similar phenomena (Fig. 5(b)), confirming that KNO_3 was the unique nitrogen source. The *operando* EIS was applied to reveal the superb activity towards urea electrosynthesis. As shown in Figs. 5(c) and 5(d), the relative Bode plots of Ni-NCNT and CuNi-NCNT showed an intensive peak at low frequency, corresponding to the urea electrosynthesis. The Bode difference between −0.1 and −0.4 V vs. RHE was larger for CuNi-NCNT than the counterpart of Ni-NCNT, underlining the excellent catalytic activity; besides, the R_{ct} of CuNi-NCNT was lower than Ni-NCNT (Fig. S24 in the ESM). The *in-situ* Raman spectroscopy of CuNi-NCNT shown in Fig. 5(e) indicated that the Ni–H bond was

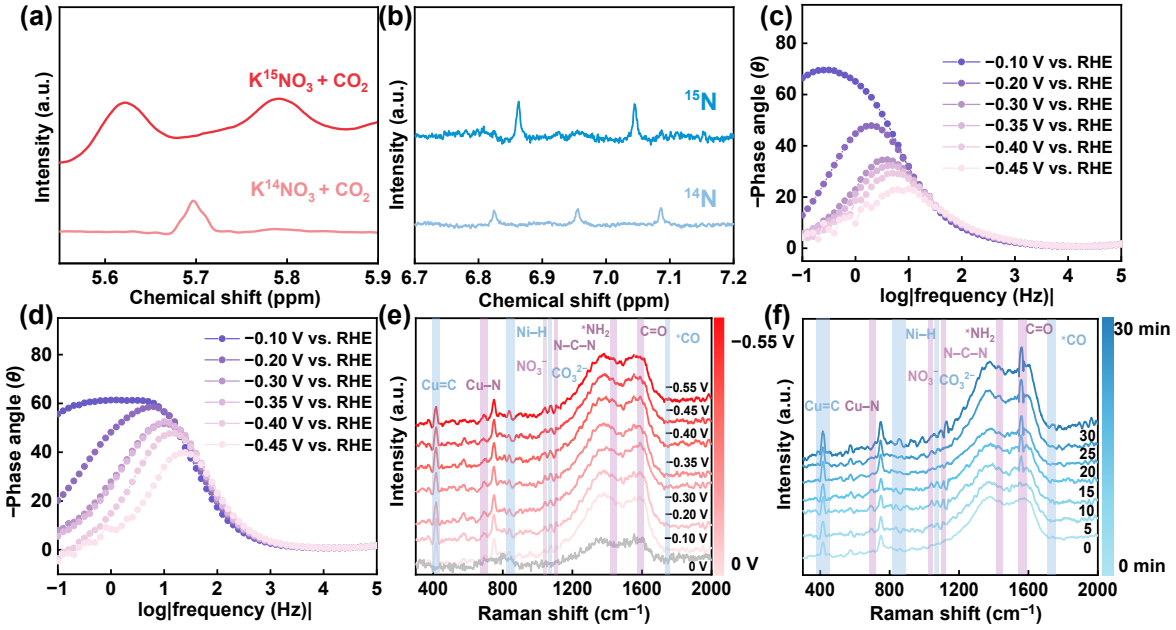

Figure 5 ((a) and (b)) ^{1}H NMR spectra of (a) urea and (b) NH_4^+ synthesized from ^{15}N- and ^{14}N-labeled KNO_3. ((c) and (d)) *In-situ* EIS of (c) CuNi-NCNT and (d) Ni-NCNT. ((e) and (f)) *In-situ* Raman spectra of CuNi-NCNT under (e) different voltages and (f) reaction times.

detected at 830 cm^{-1} with the increment in applied potential, suggesting that Ni atoms were active for hydrogen adsorption [46]. Cu–N bond was detected at 689 cm^{-1}, suggesting the electrochemical adsorption of NO_3^- on Cu atoms [47]. In addition, the Cu=C bond was detected at 414 cm^{-1}, implying the CO_2 adsorbed on Cu atoms [48]. The NO_3^- and dissolved CO_3^{2-} were detected at 1042 and 1076 cm^{-1}, respectively. It was noticed that the NO_3^- was reduced to NH_2, evidenced by Raman peak at 1437 cm^{-1} [49]; consequently, the CO_2 was deoxygenated to CO detected at 1752 cm^{-1}. Therefore, the C–N coupling occurred and N–C–N structure was found at 1107 cm^{-1}, which was not observed for CuNi-NCNT [24]. Moreover, the C=O bond originated from urea was also detected at 1549 cm^{-1}, implying the C–N coupling during electrocatalysis [50, 51]. Additionally, the Raman spectroscopy was recorded after various durations (Fig. 5(f)). It was found that the intensity of C=O bond was increased due to the accumulation in urea; additionally, the signal of *NH_2 and *CO also became strong, indicating the simultaneous formation of NH_2 and CO contributing to a robust urea electrosynthesis [19]. The Raman spectroscopy revealed that hydrogen atoms and CO_2/NO_3^- were prone to be adsorbed on Ni and Cu sites, respectively, leading to a superior capability for urea electrosynthesis.

3.3 Theoretical calculation

DFT calculations were further employed to elucidate the mechanism. As shown in Fig. 6(a), total density of state (TDOS) of Ni(111), Cu(111), and CuNi was calculated and the corresponding d-band center is displayed in Fig. 6(b). It was noticed that the d-band center of Cu was upshifted for CuNi with relative to Cu(111), demonstrating that the NO_3^- and CO_2 adsorption was enhanced on Cu sites; in contrast, a downshift was found for d-band center of Ni in CuNi with relative to Ni(111), indicating weakened binding strength with hydrogen atom to hydrogenate the adsorbed NO_3^- and CO_2 on adjacent Cu. During urea electrosynthesis, the electron would transfer from the $d_{x^2-y^2}$ orbital of the active site to reactant. As shown in Fig. 6(c), the width of $d_{x^2-y^2}$ orbital was higher for CuNi than Ni(111) and Cu(111); as a result, the electron was more prone to transfer to the reactant to accelerate the reaction kinetics [52]. In addition, HER catalysis is the competitive reaction in urea electrosynthesis. The Gibbs free energy for hydrogen (ΔG_{H^*}) value was −0.40 and −0.21 eV for Ni(111) and Cu(111), respectively (Fig. 6(d)). To verify the steric effect on HER catalysis, the ΔG_{H^*} values were calculated for the CuNi structure, in which Cu adsorbed NO_3^- and CO_2. It was found that hydrogen atom was difficult to adsorb on Ni site. Due to the shift in d-band center, Cu and Ni atoms performed ΔG_{H^*} values of −0.26 and −0.33 eV, respectively. However, the binding strength between Cu and NO_3^- was stronger with formation energy of −0.37 eV. Thus, the HER catalysis was suppressed for CuNi during urea electrosynthesis. Crystal orbital Hamilton population (COHP) can reveal bonding strength. As shown in Fig. S25 in the ESM, the −ICOHP values of Ni(111), Cu(111), and CuNi were 0.18, 0.14, and 0.15 eV, respectively. The Cu–Ni bond was stronger than Cu–Cu bond. As shown in Fig. 6(e), higher −ICOHP values were found for Cu–N and Cu–C than Cu–H in CuNi, indicating that NO_3^- was more prone to adsorb on Cu; moreover, the −ICOHP values were decreased for Ni atom in CuNi structure (Fig. 6(f)), strongly supporting the hydrogen atom adsorbed on Ni atom [53]. The reaction intermediates on active sites for urea electrosynthesis are displayed in Fig. S26 in the ESM. As shown in Fig. 6(g), the rate limiting step involved the coupling of C–N bond, and the energy barrier for Cu(111), Ni(111), and CuNi was 1.16, 1.14, and 0.55 eV in urea synthesis, respectively. Therefore, a robust catalytic activity towards urea electrosynthesis was achieved for CuNi due to the broken continuous hydrogen adsorption sites, in which hydrogen atom and NO_3^- were prone to electrochemically adsorb on Ni and Cu atoms.

4 Conclusions

In summary, we designed and synthesized CuNi alloy nanoparticles encapsulated into nitrogen doped carbon nanotubes for

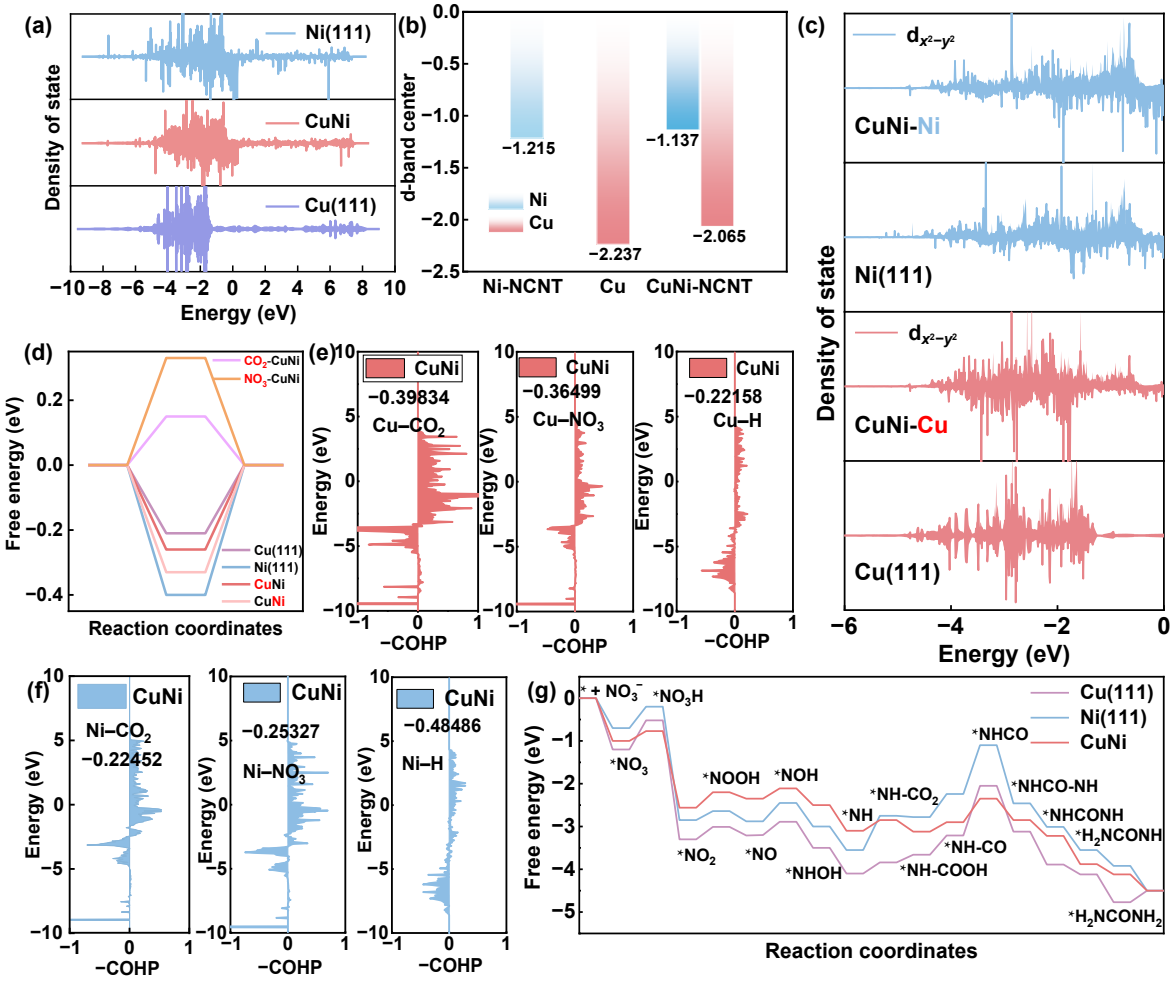

Figure 6 (a) Density of state, (b) d-band center, and (c) $d_{x^2-y^2}$ orbital of Cu(111), Ni(111), and CuNi. (d) Comparison of ΔG_H adsorption on different sites. ((e) and (f)) Comparison of COHP for CO_2, NO_3^-, and H on (e) Cu and (f) Ni atoms in CuNi. (g) Step diagrams of CuNi, Cu(111), and Ni(111) in the electrochemical synthesis of urea from NO_3^- and CO_2.

electrochemical synthesis of urea. The introduction of Cu efficiently hindered the continuous hydrogen adsorption sites, blocking Tafel slope of HER; moreover, the adsorbed NO_3^-/CO_2 on Cu atom restrained the Heyrovsky step on Ni atoms via steric effect; therefore, the competitive HER catalysis was well suppressed. More importantly, the Cu sites adsorbed NO_3^- favorably, contributing to a robust catalytic activity toward urea electrosynthesis with Faradaic efficiency of 33.6%. The *in-situ* Raman spectroscopy detected Ni–H, Cu=C, and Cu–N bonds at 830, 689, and 414 cm^{-1}, strongly witnessing the electrochemical adsorptions of hydrogen atom and CO_2/NO_3^- on Ni and Cu, respectively. The COHP also suggested the separative adsorption of hydrogen and CO_2/NO_3^- in CuNi alloy structure, triggering a lowered energy barrier for C–N coupling.

Electronic Supplementary Material: Supplementary material (TEM images of Ni-NCNT, cyclic voltammetry curves of Ni-NCNT and CuNi-NCNT, and UV–vis spectroscopies of Ni-NCNT and CuNi-NCNT) is available in the online version of this article at https://doi.org/10.26599/NR.2026.94908834.

Data availability

All data needed to support the conclusions in the paper are presented in the manuscript and the Electronic Supplementary Material. Additional data related to this paper may be requested from the corresponding author upon request.

Acknowledgements

Z. H. Y. gratefully acknowledges the 111 Project of China (No. D20015). F. L. gratefully acknowledges support from the National Natural Science Foundation of China (No. 22209126), X. Y. F. gratefully acknowledges support from the China National Petroleum Corporation (CNPC) Innovation Found (No. 2024DQ02-0212) and the Fundamental Research Funds for the Central Universities, Peking University (No. 7100604801).

Declaration of competing interest

All the contributing authors report no conflict of interests in this work.

Author contribution statement

Y. H. X.: Conceptualization, experimental design, data curation, formal analysis, investigation, visualization, writing manuscript. Y. M. F.: Data curation, software. H. H.: Data curation. F. L.: Project

administration, funding acquisition. S. A. G.: Conceptualization. X. Y. F.: Data curation, funding acquisition, J. Z.: Conceptualization. Z. H. Y.: Project administration, funding acquisition, manuscript revision. All the authors have approved the final manuscript.

Use of AI statement

None.

References

[1] Shi, R.; Zhang, T. R. Electrochemical urea production directly from N_2 and CO_2 in ambient aqueous media. *Sci. China Chem.* **2020**, *63*, 1580–1581.

[2] Gong, C. T.; Peng, Y. W.; Xu, M. Q.; Wei, X. F.; Sheng, G.; Liu, J. L.; Wu, X. W.; Han, X.; Dai, F. N.; Dong, J. Q. et al. Selective electrocatalytic synthesis of urea using entangled iron porphyrins in covalent organic frameworks. *Nat. Synth.* **2025**, *4*, 720–729.

[3] Kaur, S.; Garg, K.; Gupta, D.; Kafle, A.; Dharmender, N.; Shukla, V.; Ahuja, R.; Nagaiah, T. C. Unleashing high yield urea production by pulse electrodeposition of Bi/Cu via co-reduction of N_2 and CO_2. *ACS Energy Lett.* **2025**, *10*, 85–93.

[4] Liu, C. C.; Tong, H. L.; Wang, P. F.; Huang, R.; Huang, P. L.; Zhou, G.; Liu, L. Z. The asymmetric orbital hybridization in single-atom-dimers for urea synthesis by optimizing the C–N coupling reaction pathway. *Appl. Catal. B: Environ.* **2023**, *336*, 122917.

[5] Zhang, Z.; Li, D. Y.; Tu, Y. C.; Deng, J.; Bi, H. T.; Yao, Y. C.; Wang, Y.; Li, T. S.; Luo, Y. S.; Sun, S. J. et al. Electrocatalytic synthesis of C–N coupling compounds from CO_2 and nitrogenous species. *SusMat* **2024**, *4*, e193.

[6] Liu, J. X.; Lv, X. S.; Ma, Y. D.; Smith, S. C.; Gu, Y. T.; Kou, L. Z. Electrocatalytic urea synthesis via N_2 dimerization and universal descriptor. *ACS Nano* **2023**, *17*, 25667–25678.

[7] Pei, Y. H.; Li, D.; Pei, Y. F.; Li, Z. M.; Liu, Y. T.; Ling, X.; Lu, Y. Y.; Zhang, B. Tailoring the triple-phase microenvironment for kinetically matched C–N coupling in urea electrosynthesis. *Appl. Catal. B: Environ. Energy* **2026**, *382*, 125939.

[8] Miao, R. P.; Qin, X. P.; Wang, Y. J.; Wang, S. Q.; Gu, K. Z.; Zhou, Y. Y.; Chen, D. W.; Yan, D. F.; Gao, W. Q.; Liu, Q. H. et al. Closing electron transfer loop to boost electrocatalytic urea synthesis. *Angew. Chem., Int. Ed.* **2025**, *64*, e202517450.

[9] Zhang, Y.; Fan, X. Y.; He, X.; Yan, T. Y.; Yao, Y. C.; Zheng, D. D.; Zhao, J. X.; Cai, Q. H.; Liu, Q.; Li, L. M. et al. Ambient electrosynthesis of urea from carbon dioxide and nitrate over Mo_2C nanosheet. *Chin. Chem. Lett.* **2024**, *35*, 109806.

[10] Fu, S. Y.; Chu, K. B.; Guo, M. H.; Wu, Z. Z.; Wang, Y.; Yang, J. R.; Lai, F. L.; Liu, T. X. Ultrasonic-assisted hydrothermal synthesis of RhCu alloy nanospheres for electrocatalytic urea production. *Chem. Commun.* **2023**, *59*, 4344–4347.

[11] Yuan, J. L.; Hu, L.; Huang, J.; Chen, Y. Q.; Qiao, S. S.; Xie, H. B. Photo/electrochemical urea synthesis via CO_2 coupling with nitrogenous small molecules: Status and challenges for the development of mechanism and catalysts. *Appl. Catal. B: Environ.* **2023**, *339*, 123146.

[12] Wu, Q.; Dai, C. C.; Meng, F. X.; Jiao, Y.; Xu, Z. J. Potential and electric double-layer effect in electrocatalytic urea synthesis. *Nat. Commun.* **2024**, *15*, 1095.

[13] Wei, X. X.; Wen, X. J.; Liu, Y. Y.; Chen, C.; Xie, C.; Wang, D. D.; Qiu, M. Y.; He, N. H.; Zhou, P.; Chen, W. et al. Oxygen vacancy-mediated selective C–N coupling toward electrocatalytic urea synthesis. *J. Am. Chem. Soc.* **2022**, *144*, 11530–11535.

[14] Jiang, M. H.; Zhu, M. F.; Wang, M. J.; He, Y.; Luo, X. J.; Wu, C. J.; Zhang, L. Y.; Jin, Z. Review on electrocatalytic coreduction of carbon dioxide and nitrogenous species for urea synthesis. *ACS Nano* **2023**, *17*, 3209–3224.

[15] Hou, T.; Ding, J. Y.; Zhang, H.; Chen, S. S.; Liu, Q.; Luo, J.; Liu, X. J. $FeNi_3$ nanoparticles for electrocatalytic synthesis of urea from carbon dioxide and nitrate. *Mater. Chem. Front.* **2023**, *7*, 4952–4960.

[16] Huang, D. S.; Qiu, X. F.; Huang, J. R.; Mao, M.; Liu, L. M.; Han, Y.; Zhao, Z. H.; Liao, P. Q.; Chen, X. M. Electrosynthesis of urea by using Fe_2O_3 nanoparticles encapsulated in a conductive metal-organic framework. *Nat. Synth.* **2024**, *3*, 1404–1413.

[17] Wang, Y. J.; Chen, D. W.; Chen, C.; Wang, S. Y. Electrocatalytic urea synthesis via C–N coupling from CO_2 and nitrogenous species. *Acc. Chem. Res.* **2024**, *57*, 247–256.

[18] Liang, J. Y.; Deng, S. J.; Li, Z. Y.; Zhou, M.; Wang, S.; Su, Y. Q.; Yang, S.; Li, H. Spin state modulation with oxygen vacancy orientates C/N intermediates for urea electrosynthesis of ultrahigh efficiency. *Adv. Mater.* **2025**, *37*, 2418828.

[19] Chen, L. Y.; Yang, S.; Yao, S. Y.; Si, Z. H.; Ding, G. C.; Zhan, P.; Song, J.; Cui, M.; Lu, L.; Qin, P. Y. Modulating adsorption configuration of intermediates on Cu-In dual-atom catalyst for boosted urea electrosynthesis. *Appl. Catal. B: Environ. Energy* **2025**, *379*, 125710.

[20] Qiu, W. B.; Qin, S. M.; Li, Y. B.; Cao, N.; Cui, W. R.; Zhang, Z. D.; Zhuang, Z. C.; Wang, D. S.; Zhang, Y. Overcoming electrostatic interaction via pulsed electroreduction for boosting the electrocatalytic urea synthesis. *Angew. Chem., Int. Ed.* **2024**, *63*, e202402684.

[21] Wan, C. Z.; Ling, Y. S.; Wang, S. B.; Pu, H. T.; Huang, Y.; Duan, X. F. Unraveling and resolving the inconsistencies in tafel analysis for hydrogen evolution reactions. *ACS Cent. Sci.* **2024**, *10*, 658–665.

[22] Zhang, S. B.; Geng, J.; Zhao, Z.; Jin, M.; Li, W. Y.; Ye, Y. X.; Li, K.; Wang, G. Z.; Zhang, Y. X.; Yin, H. J. et al. High-efficiency electrosynthesis of urea over bacterial cellulose regulated Pd-Cu bimetallic catalyst. *EES Catal.* **2023**, *1*, 45–53.

[23] Zhu, X. R.; Li, Y. F. Insights into the structure-sensitive catalytic performance of palladium-copper alloys in electrochemical urea synthesis. *ACS Catal.* **2023**, *13*, 15322–15330.

[24] Feng, P. Y.; Wang, S.; Dai, Z. C.; Chen, Y. X.; Zhang, B. C.; Cheng, M. Y.; Ke, B. Q.; Xia, J.; Zhang, G. Q.; Huang, F. Q. Stable $Cu^{\delta+}$ sites derived from analogous rectifying interface in AgCu biphasic aerogels for efficient urea electrosynthesis at low potential. *Nat. Commun.* **2026**, *17*, 59.

[25] Xiao, Y.; Yang, X.; Yang, Y. B.; Sun, C.; Shen, C.; Zhang, Y.; Han, L. L. CuAg alloy catalyst for modulating the activity of C–N coupling toward acetamide and urea synthesis via explicit pH-dependent water and induced ionic liquid cations models. *ACS Catal.* **2025**, *15*, 19552–19565.

[26] Zhang, X.; Sun, H.; Wang, Y. R.; Shi, Z.; Zhong, R. L.; Sun, C. Y.; Liu, J. Y.; Su, Z. M.; Lan, Y. Q. Dynamic control of asymmetric charge distribution for electrocatalytic urea synthesis. *Adv. Mater.* **2024**, *36*, 2408510.

[27] Zhao, C.; Jin, Y.; Yuan, J. K.; Hou, Q. L.; Li, H.; Yan, X. Q.; Ou, H. H.; Yang, G. D. Tailoring activation intermediates of CO_2 initiates C–N coupling for highly selective urea electrosynthesis. *J. Am. Chem. Soc.* **2025**, *147*, 8871–8880.

[28] Yu, Y. C.; Ma, X. D.; Huang, Y. M.; Jiao, M. G.; Kong, L. J.; Zhang, B. Defect-induced triple synergistic modulation of CuBi clusters for enhanced urea electrosynthesis. *Angew. Chem., Int. Ed.* **2026**, *138*, e25147.

[29] Song, X. N.; Ma, X. D.; Chen, T. H.; Xu, L.; Feng, J. Q.; Wu, L. M.; Jia, S. H.; Zhang, L. B.; Tan, X. X.; Wang, R. H. et al. Urea synthesis via coelectrolysis of CO_2 and nitrate over heterostructured Cu-Bi catalysts. *J. Am. Chem. Soc.* **2024**, *146*, 25813–25823.

[30] Xu, Y. X.; Chen, X. Y.; Yuan, Q. X.; Wu, Y. H.; Wang, K.; Sun, K.; Zhang, J. F.; Wu, J. J.; Jiang, J. C.; Fan, M. M. Boron crystal nanostructure induced $*NH_2$ spilling over boron modified Cu catalyst to greatly enhance urea synthesis at a low overpotential. *Appl. Catal. B: Environ. Energy* **2026**, *384*, 126164.

[31] Yin, Y. Y.; Ling, Z. N.; Liu, S. Q.; Wang, Y. Y.; Zhao, W. L.; Wang, H. G.; Yang, J. H.; Feng, R. J.; Zhang, S. P.; Xing, X. Q. et al.

Efficient urea electrosynthesis from CO_2 and nitrate mediated by an ionic liquid bridge. *Nat. Sustain.* **2026**, *9*, 108–116.

[32] Wu, G.; Zelenay, P. Activity versus stability of atomically dispersed transition-metal electrocatalysts. *Nat. Rev. Mater.* **2024**, *9*, 643–656.

[33] Xu, M. Q.; Xue, Y. Y.; Liu, Z. Z.; Lv, X. M.; Han, Q.; Zheng, G. F. Efficient urea electrosynthesis on a Cu_3 molecular catalyst with dynamically adaptive intercopper spacings. *J. Am. Chem. Soc.* **2025**, *147*, 41956–41964.

[34] Zhang, Q.; Luo, F.; Long, X.; Yu, X. X.; Qu, K. G.; Yang, Z. H. N, P doped carbon nanotubes confined WN-Ni Mott–schottky heterogeneous electrocatalyst for water splitting and rechargeable zinc-air batteries. *Appl. Catal. B: Environ.* **2021**, *298*, 120511.

[35] Zhang, Q.; Kazim, F. M. D.; Ma, S. X.; Qu, K. G.; Li, M.; Wang, Y. G.; Hu, H.; Cai, W. W.; Yang, Z. H. Nitrogen dopants in nickel nanoparticles embedded carbon nanotubes promote overall urea oxidation. *Appl. Catal. B: Environ.* **2021**, *280*, 119436.

[36] Xie, Y. H.; Feng, Y. M.; Pan, S. Y.; Bao, H. F.; Yu, Y. J.; Luo, F.; Yang, Z. H. Electrochemical leaching of Ni dopants in IrRu alloy electrocatalyst boosts overall water splitting. *Adv. Funct. Mater.* **2024**, *34*, 2406351.

[37] Zhang, B. C.; Chen, Y. X.; Dai, Z. C.; Cheng, M. Y.; Feng, P. Y.; Ke, B. Q.; Zhang, G. Q. Intrinsic Ni^0–$Ni^{\delta+}$ pairs in anti-perovskite $NiNNi_3$ act as hydrogen radical emitters for Cu enabling promoted electrocatalytic nitrate reduction. *Angew. Chem., Int. Ed.* **2026**, *138*, e21064.

[38] Liu, X.; Pang, H. Y.; Kou, X. R.; Tang, Z.; Cui, B.; Cen, S. H.; Wei, Y. C. Synergistic interaction of ternary Pd−Cu−Ni confined in nanoparticles as pH-universal catalysts for enhanced hydrogen evolution reaction. *Chin. Chem. Lett.* **2026**, *37*, 111567.

[39] Du, J. X.; Wu, Y. S.; Fang, S. Y.; Xu, D. L.; Liu, M.; Liang, H.; Wu, Z. B.; Lu, G. M.; Wu, X. H. Nano-confinement engineering boosts C–N coupling for urea electrosynthesis. *Nat. Commun.* **2025**, *17*, 1008.

[40] Li, X. W.; Ma, S. X.; Luo, F.; Yang, Z. H. Engineering oxygen vacancies in Co_3O_4 to boost p-d hybridization for hydrogeneration of nitrogen and oxygen. *Appl. Surf. Sci.* **2022**, *600*, 154115.

[41] Zhou, X.; Xu, W. C.; Liang, Y. Q.; Jiang, H.; Li, Z. Y.; Wu, S. L.; Gao, Z. H.; Cui, Z. D.; Zhu, S. L. Dynamically restructuring nanoporous Cu-Co electrocatalyst for efficient nitrate electroreduction to ammonia. *ACS Catal.* **2024**, *14*, 12251–12259.

[42] Li, Z. Y.; Zhou, P.; Zhou, M.; Jiang, H.; Li, H.; Liu, S. Q.; Zhang, H.; Yang, S.; Zhang, Z. H. Synergistic electrocatalysis of crystal facet and O-vacancy for enhancive urea synthesis from nitrate and CO_2. *Appl. Catal. B: Environ.* **2023**, *338*, 122962.

[43] Liu, J. F.; Zhang, S. B.; Mao, Z. X.; Li, W. Y.; Jin, M.; Yin, H. J.; Zhang, Y. X.; Wang, G. Z.; Zhang, H. M.; Zhao, H. J. *In-situ* electrochemical reconstruction of copper single-sites to dual-sites for ambient urea synthesis. *Angew. Chem., Int. Ed.* **2025**, *64*, e202509385.

[44] Feng, Z. H.; Zhang, L. H.; Guo, Y. B.; Guo, J. Y.; Li, F.; Yu, F. S. Charge polarization boosting electrochemical urea synthesis by co-reduction of CO_2 and nitrite in dilute concentrations with a unity carbon selectivity. *Angew. Chem., Int. Ed.* **2025**, *64*, e202500262.

[45] Yin, H. Q.; Sun, Z. S.; Zhao, Q. P.; Yang, L. L.; Lu, T. B.; Zhang, Z. M. Electrochemical urea synthesis by co-reduction of CO_2 and nitrate with Fe^{II}–Fe^{III} OOH@$BiVO_4$ heterostructures. *J. Energy Chem.* **2023**, *84*, 385–393.

[46] Li, H. M.; Li, S. P.; Guan, R. J.; Jin, Z. Y.; Xiao, D.; Guo, Y.; Li, P. P. Modulating the surface concentration and lifetime of active hydrogen in Cu-based layered double hydroxides for electrocatalytic nitrate reduction to ammonia. *ACS Catal.* **2024**, *14*, 12042–12050.

[47] Li, H.; Xu, L. T.; Bo, S. W.; Wang, Y. J.; Xu, H.; Chen, C.; Miao, R. P.; Chen, D. W.; Zhang, K. F.; Liu, Q. H. et al. Ligand engineering towards electrocatalytic urea synthesis on a molecular catalyst. *Nat. Commun.* **2024**, *15*, 8858.

[48] Yang, Y.; Zhang, W. J.; Wu, G. C.; Huang, Q.; Wen, J. H.; Wang, D. S.; Liu, M. Y. Electronic structure tuning in Cu-Co dual single atom catalysts for enhanced COOH* spillover and electrocalytic CO_2 reduction activity. *Angew. Chem., Int. Ed.* **2025**, *64*, e202504423.

[49] Kim, H.; Lim, T. J.; Eom, H. H.; Kim, Y. J.; Kim, K.; Lee, J. W. Reconstructed fluorine doped perovskites for electrocatalytic urea production through reaction pathways with CO_2 and nitrate ions. *Appl. Catal. B: Environ. Energy* **2025**, *365*, 124974.

[50] Ge, X.; Yuan, J. L.; Li, H.; Wang, L.; Xie, H. B.; Liu, C. B. Enhancing *CO and *N≡N orbital coupling via tuned mn d-p hybridization at MnO/Mn_7C_3 interfaces for highly selective urea electrosynthesis. *Adv. Energy Mater.* **2025**, *15*, e03375.

[51] Deng, T.; Jia, S. Q.; Xue, C.; Cheng, H. L.; Jiao, J. P.; Chen, X.; Xia, Z. H.; Dong, M. K.; Chen, C. J.; Wu, H. H. et al. Phosphorus-doped Cu/Fe_2O_3 electrocatalysts with optimized synergy between the different sites for efficient urea electrosynthesis. *J. Am. Chem. Soc.* **2025**, *147*, 32924–32931.

[52] Li, J. H.; Wu, C.; Wang, Z.; Meng, H. Y.; Zhang, Q.; Tang, Y.; Zou, A. Q.; Zhang, Y. M.; Zhong, H. Y.; Xi, S. B. et al. Unveiling the pivotal role of $d_{x^2-y^2}$ electronic states in nickel-based hydroxide electrocatalysts for methanol oxidation. *Angew. Chem., Int. Ed.* **2024**, *63*, e202404730.

[53] Huang, J.; Wang, Z.; Liang, J. S.; Li, X. Y.; Pietryga, J.; Ye, Z. H.; Smith, P. T.; Kulaksizoglu, A.; Mccormick, C. R.; Kim, J. et al. Accelerating the pace of oxygen evolution reaction catalyst discovery through megalibraries. *J. Am. Chem. Soc.* **2025**, *147*, 30956–30966.